LETTER

Anomalously weak Labrador Sea convection and Atlantic overturning during the past 150 years

David J. R. Thornalley[1,2]*, Delia W. Oppo[2], Pablo Ortega[3], Jon I. Robson[3], Chris M. Brierley[1], Renee Davis[1], Ian R. Hall[4], Paola Moffa-Sanchez[4], Neil L. Rose[1], Peter T. Spooner[1], Igor Yashayaev[5] & Lloyd D. Keigwin[2]

The Atlantic meridional overturning circulation (AMOC) is a system of ocean currents that has an essential role in Earth's climate, redistributing heat and influencing the carbon cycle[1,2]. The AMOC has been shown to be weakening in recent years[1]; this decline may reflect decadal-scale variability in convection in the Labrador Sea, but short observational datasets preclude a longer-term perspective on the modern state and variability of Labrador Sea convection and the AMOC[1,3–5]. Here we provide several lines of palaeo-oceanographic evidence that Labrador Sea deep convection and the AMOC have been anomalously weak over the past 150 years or so (since the end of the Little Ice Age, LIA, approximately AD 1850) compared with the preceding 1,500 years. Our palaeoclimate reconstructions indicate that the transition occurred either as a predominantly abrupt shift towards the end of the LIA, or as a more gradual, continued decline over the past 150 years; this ambiguity probably arises from non-AMOC influences on the various proxies or from the different sensitivities of these proxies to individual components of the AMOC. We suggest that enhanced freshwater fluxes from the Arctic and Nordic seas towards the end of the LIA—sourced from melting glaciers and thickened sea ice that developed earlier in the LIA—weakened Labrador Sea convection and the AMOC. The lack of a subsequent recovery may have resulted from hysteresis or from twentieth-century melting of the Greenland Ice Sheet[6]. Our results suggest that recent decadal variability in Labrador Sea convection and the AMOC has occurred during an atypical, weak background state. Future work should aim to constrain the roles of internal climate variability and early anthropogenic forcing in the AMOC weakening described here.

The AMOC comprises northward transport of warm surface and thermocline waters, and their deep southward return flow as dense waters that formed through cooling processes and sinking at high latitudes[2]. The stability of the AMOC in response to ongoing and projected climate change is uncertain. Monitoring of the AMOC during the past decade with an instrument array at 26° N has suggested that the AMOC is weakening, and that this is occurring ten times faster than would be expected from climate model projections[1]. However, it remains uncertain whether this trend is part of a longer-term decline, natural multidecadal variability, or a combination of both. Here, we develop past reconstructions of AMOC variability that can be compared directly with instrumental datasets and provide longer-term perspective.

The Labrador Sea is an important region for deep-water formation in the North Atlantic ocean[5]. Moreover, modelling studies suggest that deep-Labrador-Sea density (DLSD) might be a useful predictor of AMOC change[3,4,7]. This is because density anomalies produced in the Labrador Sea—caused predominantly by varying deep convection—can propagate southwards rapidly (on timescales of the order of months) along the western margin via boundary waves, altering the cross-basin zonal density gradient, and thus modifying geostrophic transport and therefore AMOC strength[2–4,7–9]. Building upon these studies, we show that DLSD anomalies are also associated with changes in the velocity of the deep western boundary current (DWBC) and the strength of the AMOC at 45° N in the high-resolution climate model HadGEM3-GC2 (see Methods and Fig. 1).
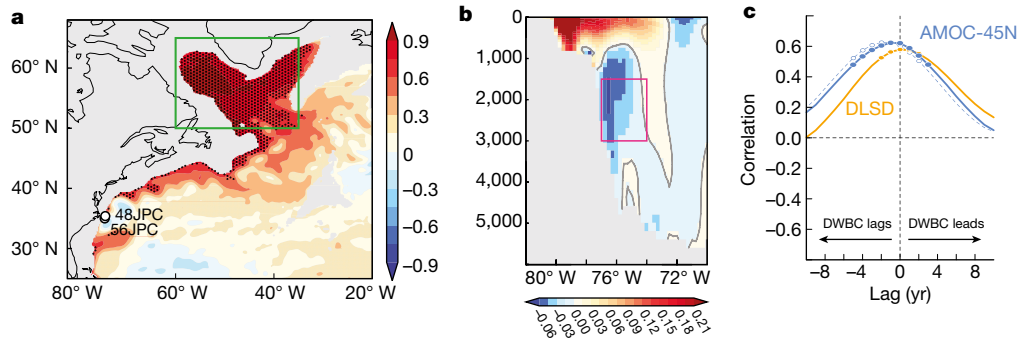
In addition to this link between the AMOC, DLSD and DWBC, changes in the AMOC also alter ocean heat transport. Modelling studies[10] suggest that AMOC weakening affects the upper-ocean heat content of the subpolar gyre (SPG) with a lag time of around ten years. Moreover, a distinct AMOC fingerprint on subsurface temperatures (T_{sub}; at depths of 400 m)[11] characterizes weak AMOC phases, with a dipole pattern of warming of the Gulf Stream extension region[12] and cooling of the subpolar Northeast Atlantic. We exploit here the model-based covariance of decadal changes in the AMOC with DLSD anomalies, SPG upper-ocean heat content and the T_{sub} fingerprint, to extend constraints on past AMOC variability (see Methods). Over the instrumental era (from AD 1950 or so), these indices suggest substantial decadal variability in the AMOC, with coherent changes in DLSD, lagged SPG upper-ocean heat content and a lagged T_{sub} AMOC fingerprint[3,5,8,10,11].

The model results in Fig. 1 suggest that we can use flow-speed reconstructions of the DWBC to infer past changes in DLSD and the AMOC. We analysed the sortable-silt mean grain size—a proxy for near-bottom current flow speed[13]—in two marine sediment cores (48JPC and 56JPC; see Methods and Extended Data Figs. 1, 2) located under the influence of southward-flowing Labrador Sea Water (LSW) within the DWBC off Cape Hatteras (hereafter DWBC$_{LSW}$). The high sediment-accumulation rates (about 0.5–1 cm per year) and the modern core-top enable direct comparison of the record from 56JPC with observational datasets (Fig. 2).

In agreement with the model-predicted relationship (Fig. 1), changes in the inferred flow speed of the DWBC$_{LSW}$ show similar, in-phase, variability with observed DLSD[5]. Moreover, there is strong covariability of our DWBC$_{LSW}$ proxy with the lagged (12-year) SPG upper-ocean heat content and T_{sub} index from observational analysis (Fig. 2a). Over the past 100 years or so, the spatial correlation of upper-ocean heat content anomalies associated with our DWBC$_{LSW}$ proxy has closely resembled the T_{sub} AMOC fingerprint (Fig. 2b, c), supporting the concept that the DWBC$_{LSW}$ proxy and upper-ocean temperature changes provide complementary, coherent information on a common phenomenon, namely, AMOC variability. Combined, these datasets indicate that decadal variability has been a dominant feature of the past 130 years, with the most recent strengthening of LSW formation during the mid-1990s, and its subsequent decline, being particularly prominent features.

To gain insight into variability before the instrumental era, we first extended our DWBC$_{LSW}$ flow-speed reconstruction (Fig. 3e). The DWBC$_{LSW}$ proxy suggests that the AMOC has been weaker during the past 150 years than at any other time during the past 1,600 years. The emergence of this weaker state (during which the smoothed record exceeds a noise threshold of 2σ pre-industrial-era variability) takes place at about AD 1880 in both cores. The overall transition

Fig. 1 | Modelled link between DWBC velocity, deep Labrador Sea density and the AMOC. a, Correlation (colour bar on the right) between the vertically averaged ocean density (1,000 m to 2,500 m) and DLSD (average ocean density between 1,000 m and 2,500 m in the area defined by the green box), as modelled using a control run of the high-resolution climate model HadGEM3-GC2. The locations of the sediment-core sites used for DWBC flow-s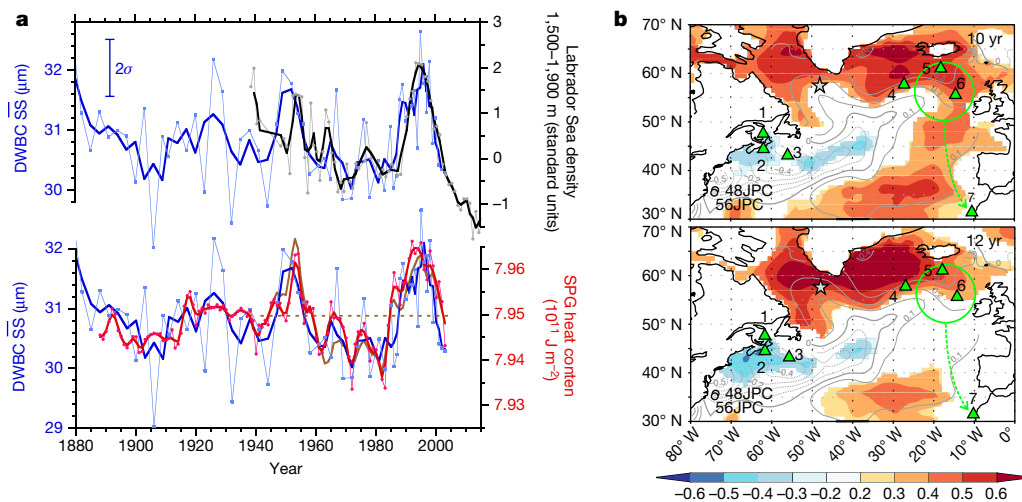peed reconstruction are also shown. **b**, Climatology of the modelled meridional ocean velocity (in metres per second; see colour bar) at 30° N to 35° N (see Methods and Extended Data Figs. 7, 8), illustrating the modelled position of the DWBC (red outline). The y axis shows water depth in metres. **c**, Cross-correlations between the modelled average DWBC flow speed from the red box in panel **b**, and indices of DLSD and the AMOC at 45° N (the dashed blue line omits the Ekman component).

occurs from about AD 1750 to AD 1900—late in the Little Ice Age (AD 1350–1850) and during the early stages of the industrial era (1830 onwards[14]). Applying the flow-speed calibration for sortable silt[13] suggests a decrease from $17\,\mathrm{cm\,s^{-1}}$ to $14.5\,\mathrm{cm\,s^{-1}}$ in core 56JPC during this transition period, and from $14\,\mathrm{cm\,s^{-1}}$ to $12\,\mathrm{cm\,s^{-1}}$ in 48JPC, suggesting a decrease in $DWBC_{LSW}$ strength of approximately 15% (assuming a constant $DWBC_{LSW}$ cross-sectional area). This decrease is equivalent to 3σ and 4σ of the pre-industrial-era variability in 48JPC and 56JPC, respectively.

Second, we compiled quantitative proxy records of subsurface ocean temperatures (at depths of about 50–200 m) from key locations to extend the T_{sub} AMOC proxy (Fig. 3a–c; see Methods and Extended Data Figs. 3, 4). This T_{sub} proxy reconstruction provides support for the proposed AMOC weakening. Opposing temperature anomalies recorded in the two regions after about AD 1830—with warming of the Gulf Stream extension region and cooling of the subpolar Northeast Atlantic region—suggest a weaker industrial-era AMOC. Further support for the AMOC weakening is suggested by the spatial pattern of T_{sub} change in the Northwest Atlantic during the onset of the industrial era (Extended Data Fig. 5). In contrast to the prominent changes recorded in our proxy reconstructions at the end of the LIA, more subdued variability occurs during the earlier part of our records (AD 400–1800). This might suggest that the forcing and AMOC response were weaker then, or that the AMOC did not play a leading role in the (multi)centennial climate variability of this period[15,16].

Labrador Sea deep convection is a major contributor to the AMOC, but susceptible to weakening[5]. This fact, combined with its role in decadal AMOC variability over the past 100 years or so (Fig. 2) and model analysis of mechanisms for AMOC variability in operation today[8], makes it likely that changes in Labrador Sea convection were involved in the weakening of the AMOC at the end of the LIA. Further correlative (although not necessarily causative) support for this idea is revealed by palaeo-oceanographic evidence from the Labrador Sea. Strong deep convection in the Labrador Sea is typically associated with cooling and freshening of the subsurface ocean[5]. Therefore, the reconstructed shift to warmer and saltier subsurface conditions in the northeast Labrador Sea[17] over the past 150 years (Fig. 3d; equivalent to around 2σ of pre-industrial-era variability) is consistent with a shift to a state characterized by reduced deep convection, with only occasional episodes of sustained deep convection. Reconstructions of the

Fig. 2 | Proxy validation and recent multidecadal variability. a, The mean grain size of sortable silt (SS; from sediment core 56JPC; blue) is compared with: the central-Labrador-Sea annual density[5] (black; $r^2 = 0.56$; $n = 54$), which is comparable to the model-based DLSD (Extended Data Fig. 9); the 12-year lagged SPG upper-ocean heat content (at 0–700 m; 55° N to 65° N, 15° W to 60° W; EN4 dataset; red; $r^2 = 0.58$; $n = 116$); and the 12-year lagged T_{sub} AMOC fingerprint[11] (brown; dashed line shows the zero line; $r^2 = 0.76$; $n = 55$). Correlations (and the 2σ SS error bar; $n = 30$) are for three-point means (thicker lines). Low-resolution 48JPC data are not shown. **b**, 10- and 12-year lagged spatial correlation (colour bar; R) of upper-ocean heat content (at 0–700 m) with reconstructed $DWBC_{LSW}$ flow speed (from sediment core 56JPC); the heat content lags behind the DWBC. Grey contours show the spatial T_{sub} AMOC proxy[11]; green triangles show T_{sub} proxy sites; the green circle marks the surface region controlling benthic temperatures at site 7; grey circles are DWBC sites; the grey star marks the core site from ref. [17].
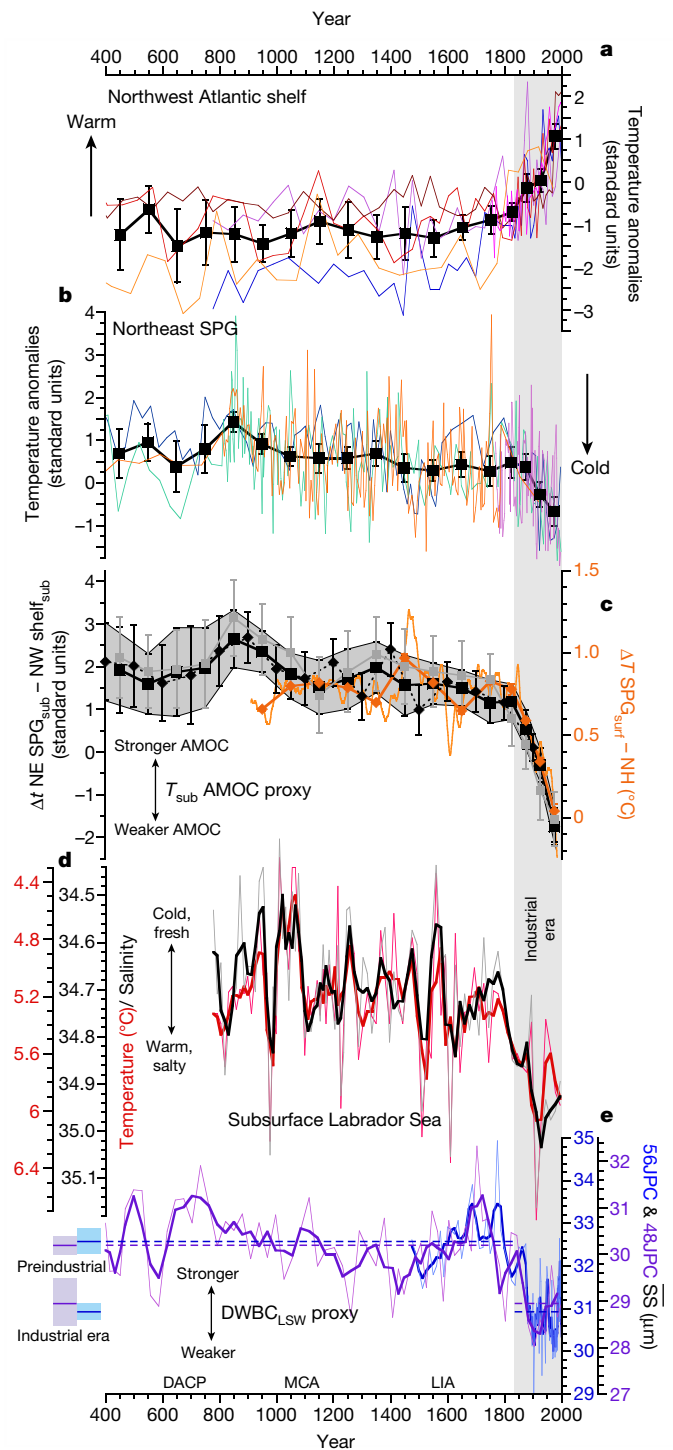
other major deep-water contributors to the AMOC—the two Nordic Seas overflows—suggest that, on centennial timescales, they have varied in anti-phase and probably therefore compensated for one another during the past 3,000 years[18]. Hence, changes in Labrador Sea deep convection may have been the main cause of AMOC variability over this period.

Although atmospheric circulation has played a dominant part in recent decadal variability in the AMOC (and LSW)[2,8], there is no strong evidence that the AMOC decrease at the end of the LIA was similarly caused by a shift in atmospheric circulation[19]. Instead, we hypothesize that the AMOC weakening was caused by enhanced freshwater fluxes associated with the melting and export of ice and freshwater from the Arctic and Nordic seas. During the LIA, circum-Arctic glaciers and multiyear Arctic and Nordic sea ice were at their most advanced state of the past few thousand years, and there were large ice shelves in the Canadian Arctic and exceptionally thick multiyear sea ice. Yet, by the early twentieth century, many of these features had disappeared or were retreating[20–23].

Modelling studies suggest that enhanced freshwater fluxes of about 10–100 mSv over a few decades can weaken Labrador Sea convection and the AMOC[24], although models with strong hysteresis of Labrador Sea convection[25] suggest that this weakening may be caused by as little as 5–10 mSv of freshwater. Unfortunately, there are few data to constrain the Arctic and Nordic Sea freshwater fluxes associated with the end of the LIA. The earliest observational datasets[26,27] suggest that a flux of about 10 mSv resulted from sea-ice loss in the Arctic and Nordic seas during 1895–1920, to which we must also add melting of previously expanded circum-Arctic glaciers and ice shelves, and enhanced melting of the Greenland Ice Sheet. Alternatively, we could estimate that a 1-m reduction in average Arctic sea-ice thickness during the termination of the LIA could have yielded a freshwater flux of 10 mSv for 50 years. Although further work is required to improve this incomplete estimate, there was probably sufficient freshwater stored in the Arctic and Nordic seas during the LIA to influence Labrador Sea convection and the AMOC.

The AMOC weakening recorded in our two marine reconstructions is broadly similar to that in a predominantly terrestrial-based AMOC proxy reconstruction[6] (Fig. 3c). Our T_{sub} AMOC proxy and that of ref. [6] (Fig. 3c) both suggest a substantial decline in the AMOC through the twentieth century, whereas our $DWBC_{LSW}$ AMOC proxy and the observational-based T_{sub} AMOC index (Fig. 2a and Extended Data Fig. 6) suggest relatively little long-term AMOC decline during this period. These differences may be attributed to several factors. First, our sediment-core-based T_{sub} proxy is subject to artificial smoothing, caused by combining numerous records with substantial (around 10–100-year) individual age uncertainties, and compounded by sediment mixing by organisms (bioturbation). Furthermore, the T_{sub} proxy sediment cores were retrieved in the late 1990s and early 2000s, and so cannot capture the strong T_{sub} index recovery from around 2000 to 2010 that reverses the earlier prolonged decline (Extended Data Fig. 6). Alternatively, the earlier, more threshold-like change in the $DWBC_{LSW}$ AMOC proxy may be due to local shifts in the position of the DWBC and/or nonlinear dynamics of the DWBC response to AMOC change. However, given the similarity of the $DWBC_{LSW}$ reconstructions from cores 56JPC and 48JPC (located at different water depths), and the strong correlation of $DWBC_{LSW}$ with Labrador Sea density and the T_{sub} AMOC index over the instrumental period, we suggest that these factors are not substantial. Finally, the differences between the AMOC reconstructions may reflect their varying response timescales and sensitivities to the different individual components of the AMOC and the SPG[28,29].

Our study raises several issues regarding the modelling of the AMOC in historical experiments. The inferred transition to a weakened AMOC occurred near the onset of the industrial era, several decades before the strongest global warming trend, and has remained weak up to the present day. This suggests either hysteresis of the AMOC in response to an early climate forcing—natural (solar, volcanic) or anthropogenic (greenhouse gases, aerosols, land-use change)—or that continued climate forcing, such as the melting of the Greenland Ice Sheet[6], has been sufficient to keep the AMOC weak or cause further weakening.

Fig. 3 | Proxy reconstructions of AMOC changes over the past 1,600 years. a, **b**, Subsurface Northwest Atlantic shelf (**a**) and Northeast Atlantic SPG (**b**) temperatures, taken at sites shown in Fig. 2b. Composite stacks are in black. **c**, Black and grey, our T_{sub} AMOC proxy with different types of binning (see Extended Data Fig. 4). Orange: AMOC proxy from Rahmstorf et al.[6]; 1 °C = 2.3 Sv; thin line, 21-year smoothing; thick line and symbols, binned as for our T_{sub} AMOC proxy. NE SPG, Northeast Atlantic subpolar gyre; NW shelf, Northwest Atlantic shelf; NH, Northern Hemisphere; sub, subsurface; surf, surface. **d**, Subsurface (around 100–200 m) temperature and salinity of the northeast Labrador Sea, based on Mg/Ca-δ^{18}O analysis of the planktic foraminifera *Neogloboquadrina pachyderma*[17]. **e**, Sortable silt (SS) mean grain size. Blue, core 56JPC; purple, 48JPC; bold, three-point means; dashed lines, industrial/pre-industrial era averages; error bars/shading, ±2 s.e. DACP, Dark Ages Cold Period (around AD 400–800); MCA, Mediaeval Climate Anomaly (around AD 900–1250).

Our reconstructions also differ from most climate model simulations, which show either negligible AMOC change or a later, more gradual reduction[30]. Many factors may be responsible for this model–data discrepancy: a misrepresentation of AMOC-related processes and possible hysteresis, including underestimation of AMOC sensitivity to climate (freshwater) forcing[29,31]; the underestimation or absence of important freshwater fluxes during the end of the LIA; and the lack of transient forced behaviour in the 'constant forcing' pre-industrial controls used to initialize historical forcings. Resolving these issues will be important for improving the accuracy of projected changes in the AMOC.

In conclusion, our study reveals an anomalously weak AMOC over the past 150 years or so. Because of its role in heat transport, it is often assumed that AMOC weakening cools the Northern Hemisphere. However, our study demonstrates that changes in the AMOC are not always synchronous with temperature changes. That AMOC weakening occurred during the late LIA and onset of the industrial era, rather than earlier in the LIA, may point to additional forcing factors at this time, such as an increase in the export of thickened Arctic and Nordic sea ice, or the melting of circum-Arctic ice shelves. The persistence of a weak AMOC during the twentieth century, when there was pronounced Northern Hemisphere and global warming, suggests that other climate forcings—such as greenhouse gas warming—were dominant during this period. We therefore infer that the AMOC has responded to recent centennial-scale climate change, rather than driven it. Regardless, the weak state of the AMOC over the past 150 years may have modified northward ocean heat transport, as well as atmospheric warming by altering ocean–atmosphere heat transfer[32,33], underscoring the need for continued investigation of the role of the AMOC in climate change. Determining the future behaviour of the AMOC will depend in part on constraining its sensitivity and possible hysteresis to freshwater input, for which improved historical estimates of these fluxes during the AMOC weakening reported here will be especially useful.

Online content

Any Methods, including any statements of data availability and Nature Research reporting summaries, along with any additional references and Source Data files, are available in the online version of the paper at https://doi.org/10.1038/s41586-018-0007-4.

1. Srokosz, M. A. & Bryden, H. L. Observing the Atlantic Meridional Overturning Circulation yields a decade of inevitable surprises. *Science* **348**, 1255575 (2015).
2. Buckley, M. W. & Marshall, J. Observations, inferences, and mechanisms of the Atlantic Meridional Overturning Circulation: a review. *Rev. Geophys.* **54**, 5–63 (2016).
3. Jackson, L. C., Peterson, K. A., Roberts, C. D. & Wood, R. A. Recent slowing of Atlantic overturning circulation as a recovery from earlier strengthening. *Nat. Geosci.* **9**, 518–522 (2016).
4. Robson, J., Hodson, D., Hawkins, E. & Sutton, R. Atlantic overturning in decline? *Nat. Geosci.* **7**, 2–3 (2014).
5. Yashayaev, I. Hydrographic changes in the Labrador Sea, 1960–2005. *Prog. Oceanogr.* **73**, 242–276 (2007).
6. Rahmstorf, S. et al. Exceptional twentieth-century slowdown in Atlantic Ocean overturning circulation. *Nat. Clim. Change* **5**, 475–480 (2015); corrigendum **5**, 596 (2015).
7. Hodson, D. L. R. & Sutton, R. T. The impact of resolution on the adjustment and decadal variability of the Atlantic meridional overturning circulation in a coupled climate model. *Clim. Dyn.* **39**, 3057–3073 (2012).
8. Ortega, P., Robson, J., Sutton, R. T. & Andrews, M. B. Mechanisms of decadal variability in the Labrador Sea and the wider North Atlantic in a high-resolution climate model. *Clim. Dyn.* **49**, 2625–2647 (2016).
9. Roberts, C. D., Garry, F. K. & Jackson, L. C. A multimodel study of sea surface temperature and subsurface density fingerprints of the Atlantic Meridional Overturning Circulation. *J. Clim.* **26**, 9155–9174 (2013).
10. Robson, J., Ortega, P. & Sutton, R. A reversal of climatic trends in the North Atlantic since 2005. *Nat. Geosci.* **9**, 513–517 (2016).
11. Zhang, R. Coherent surface-subsurface fingerprint of the Atlantic meridional overturning circulation. *Geophys. Res. Lett.* **35**, L20705 (2008).
12. Saba, V. S. et al. Enhanced warming of the Northwest Atlantic Ocean under climate change. *J. Geophys. Res. Oceans* **121**, 118–132 (2016).
13. McCave, I. N., Thornalley, D. J. R. & Hall, I. R. Relation of sortable silt grain-size to deep-sea current speeds: calibration of the 'mud current meter'. *Deep Sea Res. I Oceanogr. Res. Pap.* **127**, 1–12 (2017).
14. Abram, N. J. et al. Early onset of industrial-era warming across the oceans and continents. *Nature* **536**, 411–418 (2016).
15. Moreno-Chamarro, E., Zanchettin, D., Lohmann, K. & Jungclaus, J. H. An abrupt weakening of the subpolar gyre as trigger for Little Ice Age-type episodes. *Clim. Dyn.* **48**, 727–744 (2017).
16. Miller, G. H. et al. Abrupt onset of the Little Ice Age triggered by volcanism and sustained by sea-ice/ocean feedbacks. *Geophys. Res. Lett.* **39**, L02708 (2012).
17. Moffa-Sánchez, P., Hall, I. R., Barker, S., Thornalley, D. J. R. & Yashayaev, I. Surface changes in the eastern Labrador Sea around the onset of the Little Ice Age. *Paleoceanography* **29**, 160–175 (2014).
18. Moffa-Sanchez, P., Hall, I. R., Thornalley, D. J. R., Barker, S. & Stewart, C. Changes in the strength of the Nordic Seas overflows over the past 3000 years. *Quat. Sci. Rev.* **123**, 134–143 (2015).
19. Ortega, P. et al. A model-tested North Atlantic Oscillation reconstruction for the past millennium. *Nature* **523**, 71–74 (2015).
20. Bradley, R. S. & England, J. H. The Younger Dryas and the sea of ancient ice. *Quat. Res* **70**, 1–10 (2008).
21. Funder, S. et al. A 10,000-year record of Arctic Ocean sea-ice variability—view from the beach. *Science* **333**, 747–750 (2011).
22. Vincent, W. F., Gibson, J. A. E. & Jeffries, M. O. Ice-shelf collapse, climate change, and habitat loss in the Canadian high Arctic. *Polar Rec.* **37**, 133–142 (2001).
23. Cabedo-Sanz, P., Belt, S. T., Jennings, A. E., Andrews, J. T. & Geirsdóttir, Á. Variability in drift ice export from the Arctic Ocean to the North Icelandic Shelf over the last 8000 years: a multi-proxy evaluation. *Quat. Sci. Rev.* **146**, 99–115 (2016).
24. Yang, Q. et al. Recent increases in Arctic freshwater flux affects Labrador Sea convection and Atlantic overturning circulation. *Nat. Comm* **7**, 10525 (2016).
25. Schulz, M., Prange, M. & Klocker, A. Low-frequency oscillations of the Atlantic Ocean meridional overturning circulation in a coupled climate model. *Clim. Past* **3**, 97–107 (2007).
26. Polyakov, I. V. et al. Arctic Ocean freshwater changes over the past 100 years and their causes. *J. Clim.* **21**, 364–384 (2008).
27. Vinje, T. Anomalies and trends of sea-ice extent and atmospheric circulation in the Nordic seas during the period 1864–1998. *J. Clim.* **14**, 255–267 (2001).
28. Drijfhout, S., Oldenborgh, G. J. V. & Cimatoribus, A. Is a decline of AMOC causing the warming hole above the North Atlantic in observed and modeled warming patterns? *J. Clim.* **25**, 8373–8379 (2012).
29. Sgubin, G., Swingedouw, D., Drijfhout, S., Mary, Y. & Bennabi, A. Abrupt cooling over the North Atlantic in modern climate models. *Nat. Comm* **8**, 14375 (2017).
30. Weaver, A. J. et al. Stability of the Atlantic meridional overturning circulation: a model intercomparison. *Geophys. Res. Lett.* **39**, L20709 (2012).
31. Liu, W., Xie, S.-P., Liu, Z. & Zhu, J. Overlooked possibility of a collapsed Atlantic Meridional Overturning Circulation in warming climate. *Sci. Adv.* **3**, e1601666 (2017).
32. Drijfhout, S. Competition between global warming and an abrupt collapse of the AMOC in Earth's energy imbalance. *Sci. Rep.* **5**, 14877 (2015).
33. Kostov, Y., Armour, K. C. & Marshall, J. Impact of the Atlantic meridional overturning circulation on ocean heat storage and transient climate change. *Geophys. Res. Lett.* **41**, 2108–2116 (2014).

Author contributions The project was conceived by D.J.R.T. The NSF project proposal was written and managed by D.W.O. and D.J.R.T. Cores 56JPC and 48JPC were collected by L.D.K. D.J.R.T. analysed and interpreted the sortable-silt data, with contributions from P.T.S. and R.D. Modelling work was carried out by P.O. and J.I.R. N.L.R. analysed spheroidal carbonaceous particles. P.T.S. carried out Monte Carlo modelling. I.Y. provided the instrumental Labrador Sea density data. D.J.R.T. wrote the first draft of the paper. All authors contributed to discussion and the final version of the manuscript.

Competing interests The authors declare no competing interests.

METHODS

Climate model investigation of AMOC and DWBC changes. The climate model used here was the UK Met Office's Global Coupled model 2.0 (HadGEM3–GC2). The ocean model for HadGEM3-GC2 is Global Ocean version 5.0, which is based on version 3.4 of the Nucleus for European Models of the Ocean model (NEMO)[34]. The ocean model has 75 vertical levels and is run at a nominal 1/4° resolution using the NEMO tri-polar grid. The atmospheric component is Global Atmosphere version 6.0 of the UK Met Office Unified Model, and is run at N216 resolution (around 60 km in mid-latitudes), with 85 vertical levels. More information about the model can be found in ref. [35]. The experiment analysed here was a 310-year control simulation of HadGEM3-GC2—that is, it includes no changes in external forcings. This experiment was previously run and analysed in ref. [8], where details of the specific model experiment are included. This coupled simulation has a relatively high spatial resolution for a more accurate representation of the boundary currents, and is sufficiently long to resolve a large number of decadal oscillations. All model data have been linearly detrended to remove any potential drift, and smoothed with a 10-year running mean in order to focus on the decadal and multidecadal variability.

We use the model-based relationships to support our interpretation of the proxy-based AMOC reconstructions, which cannot be validated with the limited observations available. We chose the AMOC at 45° N because this is the latitude with the largest correlations with both the DLSD and the DWBC velocity index in the model. AMOC indices defined at other latitudes (for example, 35° N or 40° N) produce weaker, but still substantial, correlations with both DLSD and the DWBC. The simulated DWBC velocity index is the average of that at 30° N to 35° N, because at 35° N (where the sediment cores were taken) the DWBC is found offshore, which we believe is associated with the model's Gulf Stream separating further north than in the observations (Extended Data Fig. 7). We note, however, that changes in the position of the observed Gulf Stream do not appear to directly control the reconstructed flow-speed changes in the DWBC$_{LSW}$ (Extended Data Fig. 10).

We have also assessed the robustness of the model-based relationships to the smoothing. For example, we reproduced the cross-correlation analysis in Fig. 1c using undetrended and/or unsmoothed data instead. In all cases, the lead–lag relationships are similar, with larger correlations emerging when the decadal smoothing is applied. Furthermore, we also tested the sensitivity of the model-based relationships to the specific model used. In particular, we repeated the analysis of Fig. 1 in the 340-year control experiment using the HiGEM climate model[36]. HiGEM has a similar horizontal ocean resolution (1/3°), but is based on a different ocean model. Encouragingly, Extended Data Fig. 8 shows that the results are consistent across the two models, in particular the link between DLSD and the DWBC, and between the DWBC and the AMOC at 45° N. However, there are some caveats. For example, both models' Gulf Streams separate too far north, which led us to define the DWBC flow indices slightly south of the core sites. HiGEM also has a deeper DWBC than that of HadGEM3-GC2. Therefore, the DWBC index was computed at different levels in both models to represent the link between DLSD and the DWBCs. However, despite these differences, both models support the general interpretation that the DWBC in the vicinity of Cape Hatteras is strongly connected to changes in the DLSD and the AMOC.

The interpretation of the model results is consistent with previously published model studies (both low and high resolution) that have revealed a coupling between the AMOC and/or Labrador Sea density, and the DWBC[3,7,11,37]. These modelled relationships support a causal link for the correlations between the instrumental records of Labrador Sea density and the reconstructed DWBC velocity, presented in Fig. 2. Furthermore, recent instrumental data for the DWBC at 39° N from 2004 to 2014 reveal that a reduction in the velocity of classical LSW within the DWBC is also accompanied by a decrease in its density[38], as hypothesized here. The observed decrease in the velocity and density of classical LSW within the DWBC between 2004 and 2014 is also consistent with the decrease in the DLSD over this period (Fig. 2a and Extended Data Fig. 9), although a longer observational DWBC time series is needed to gain confidence in this relationship.

Age models. New and updated age models for the cores are presented in Extended Data Figs. 1 and 2, and are based on ^{14}C, ^{210}Pb and spheroidal carbonaceous particle (SCP) concentration profiles[39].

Sortable silt data. We used two marine sediment cores for DWBC flow-speed reconstruction: KNR-178-56JPC (at 35° 28′ N, 74° 43′ W, 1,718 m water depth) and KNR-178-48JPC (35° 46′ N, 74° 27′ W, 2,009 m water depth). Sediments were processed using established methods[40], taking 1-cm-wide samples at every 1 cm for the top 63 cm and then every 4 cm down to 200 cm in 56JPC, and every 1 cm down to 71 cm in 48JPC. Samples were analysed at Cardiff University on a Beckman Coulter Multisizer 4 using the Enhanced Performance Multisizer 4 beaker and stirrer setting 30 to ensure full sediment suspension. Two or three separate aliquots were analysed for each sample, sizing 70,000 particles per aliquot. Analytical precision was approximately 1% ($\pm 0.3\,\mu$m), while full procedural error

(based on replicates of about 25% of samples, starting from newly sampled bulk sediment) was $\pm 0.8\,\mu$m.

Temperature data and constructing the T_{sub} index. Numerous studies have suggested that AMOC variability is associated with a distinct surface or subsurface (400 m) temperature fingerprint in the North Atlantic[6,11,28,41]. However, the lack of long-term observations of the AMOC prevents accurate diagnosis of the precise AMOC temperature fingerprint, and models display a range of different AMOC temperature fingerprints[9,42]. Here we focus on the T_{sub} AMOC fingerprint, proposed by Zhang[11] on the basis of covariance between a modelled AMOC, the spatial pattern of the leading mode of subsurface (400 m) temperature variability, and sea-surface height changes. These model-based relationships are supported by similar relationships (spatial and temporal) observed in recent instrumental data of subsurface temperature and sea-surface height. The agreement between our DWBC$_{LSW}$ AMOC reconstruction, observed Labrador Sea density changes, and the T_{sub} AMOC fingerprint provides support for our approach and suggests that the T_{sub} AMOC fingerprint is capturing an important component of deep AMOC variability. Differences between the various proposed AMOC temperature fingerprints probably reflects their sensitivity to different aspects of the AMOC and heat transport in the North Atlantic (for example, the AMOC versus SPG circulation[28]); the temperature response to each of these components may be resolved if more comprehensive spatial networks of past North Atlantic temperature variability are generated[43].
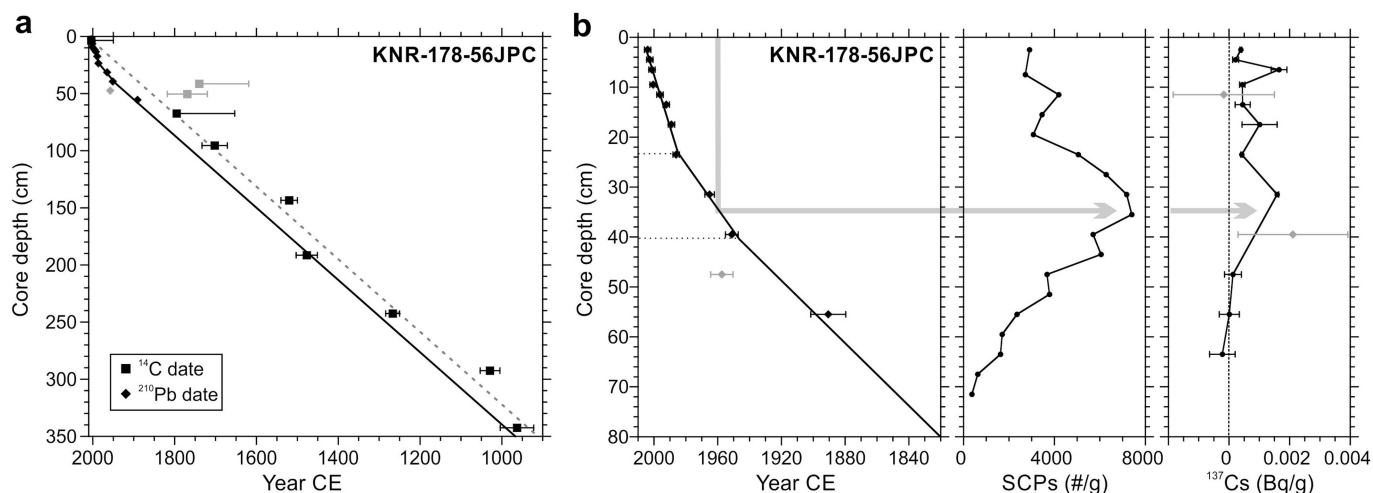
We selected records used in the OCEAN 2 K synthesis[44] from the Northwest Atlantic slope and the subpolar Northeast Atlantic, and supplemented them with additional records that also record past temperature variability in the subsurface ocean of the chosen region. We excluded cores that did not have a modern core-top age (AD 1950 or younger) or a resolution of better than 100 years. We selected foraminiferal-based temperature proxies because they record subsurface temperatures (typically at 50–200 m depth), upon which the T_{sub} proxy is based. We avoided other temperature proxies (for example, alkenones, coccolithores and diatoms) that are typically more sensitive to sea-surface temperature, rather than to T_{sub}, and which also use the fine fraction that—at the drift sites required for the necessary age resolution—contains substantial allochthonous material, compromising the fidelity of in situ temperature reconstruction[45,46].

We normalized all T_{sub} records to the interval AD 1750–2000 (the length of the shortest records). We calculated the T_{sub} proxy reconstruction as the difference between the stacked temperature records of the Northwest and Northeast Atlantic. Our results are insensitive to the precise binning or stacking method (Extended Data Fig. 4). The sedimentation rates of the cores used, combined with the effects of bioturbation, mean we cannot resolve signals on timescales shorter than about 20–50 years. Age model uncertainty is estimated to be up to about 30 years for the past 150 years or so (where cores can be dated on the basis of ^{210}Pb signatures), and around 100 years for AD 400–1800 (where ^{14}C dating is relied upon). Therefore, the optimal bin intervals chosen were 50 years for AD 1800–2000, and 100 years for AD 400–1800. Results using just 50-year and 100-year bins, as well as 30-year bins for the top 200 years, are shown in Extended Data Fig. 4.

Data availability. The proxy data that support these findings are provided as Source Data for Figs. 2 and 3 and Extended Data Figs. 1, 2, 4, 5, 6 and 9, and at National Geophysical Data Center (NGDC) Paleoclimatology database (https://www.ncdc.noaa.gov/data-access/paleoclimatology-data/datasets). Model data are available from J.I.R. (j.i.robson@reading.ac.uk) upon reasonable request.
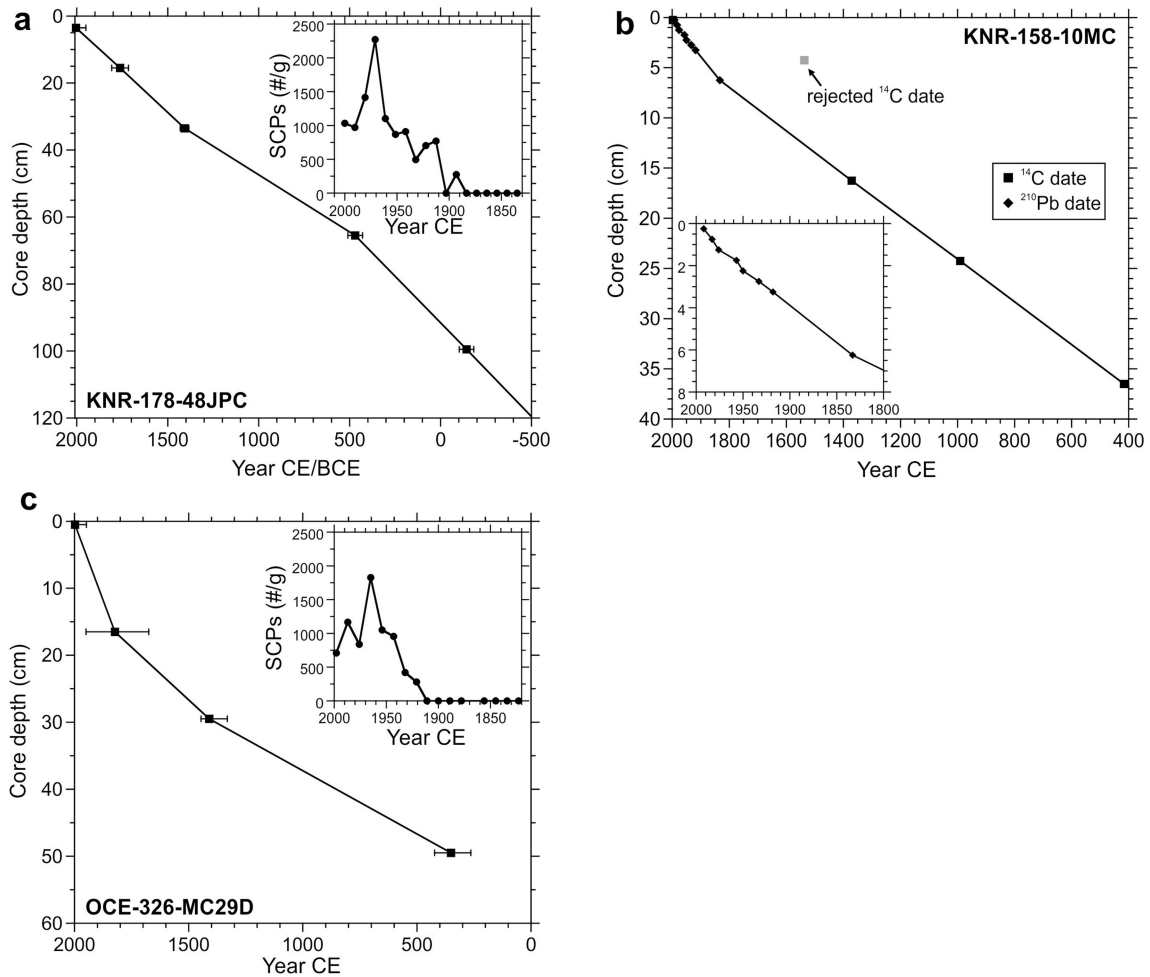
34. Megann, A. et al. GO5.0: the joint NERC–Met Office NEMO global ocean model for use in coupled and forced applications. *Geosci. Model Dev* **7**, 1069–1092 (2014).
35. Williams, K. D. et al. The Met Office Global Coupled model 2.0 (GC2) configuration. *Geosci. Model Dev* **8**, 1509–1524 (2015).
36. Shaffrey, L. C. et al. U.K. HiGEM: the new U.K. high-resolution global environment model—model description and basic evaluation. *J. Clim.* **22**, 1861–1896 (2009).
37. Bakker, P., Govin, A., Thornalley, D. J. R., Roche, D. M. & Renssen, H. The evolution of deep-ocean flow speeds and δ^{13}C under large changes in the Atlantic overturning circulation: toward a more direct model-data comparison. *Paleoceanography* **30**, 95–117 (2015).
38. Toole, J. M., Andres, M., Le Bras, I. A., Joyce, T. M. & McCartney, M. S. Moored observations of the Deep Western Boundary Current in the NWAtlantic: 2004–2014. *J. Geophys. Res. Oceans* **122**, 7488–7505 (2017).
39. Rose, N. L. Spheroidal carbonaceous fly ash particles provide a globally synchronous stratigraphic marker for the Anthropocene. *Environ. Sci. Technol.* **49**, 4155–4162 (2015).
40. McCave, I. N., Manighetti, B. & Robinson, S. G. Sortable silt and fine sediment size/composition slicing: parameters for palaeocurrent speed and palaeoceanography. *Paleoceanography* **10**, 593–610 (1995).
41. Dima, M. & Lohmann, G. Evidence for two distinct modes of large-scale ocean circulation changes over the last century. *J. Clim.* **23**, 5–16 (2010).
42. Muir, L. C. & Fedorov, A. V. How the AMOC affects ocean temperatures on decadal to centennial timescales: the North Atlantic versus an interhemispheric seesaw. *Clim. Dyn.* **45**, 151–160 (2015).

43. Ortega, P., Robson, J., Moffa-Sanchez, P., Thornalley, D. J. R. & Swingedouw, D. A last millennium perspective on North Atlantic variability: exploiting synergies between models and proxy data. *CLIVAR Exch.* **72**, 61–67 (2017).
44. McGregor, H. V. et al. Robust global ocean cooling trend for the pre-industrial Common Era. *Nat. Geosci.* **8**, 671–677 (2015).
45. McCave, I. N. A poisoned chalice? *Science* **298**, 1186–1187 (2002).
46. Filippova, A., Kienast, M., Frank, M. & Schneider, R. R. Alkenone paleothermometry in the North Atlantic: a review and synthesis of surface sediment data and calibrations. *Geochem. Geophys. Geosyst.* **17**, 1370–1382 (2016).
47. Marchitto, T. & deMenocal, P. Late Holocene variability of upper North Atlantic Deep Water temperature and salinity. *Geochem. Geophys. Geosyst.* **4**, 1100 (2003).
48. Keigwin, L. D., Sachs, J. P. & Rosenthal, Y. A. 1600-year history of the Labrador Current off Nova Scotia. *Clim. Dyn.* **21**, 53–62 (2003).
49. Keigwin, L. D. & Pickart, R. S. Slope water current over the Laurentian Fan on interannual to millennial time scales. *Science* **286**, 520–523 (1999).
50. Genovesi, L. et al. Recent changes in bottom water oxygenation and temperature in the Gulf of St. Lawrence: micropaleontological and geochemical evidence. *Limnol. Oceanogr.* **56**, 1319–1329 (2011).
51. Hall, I. R., Boessenkool, K. P., Barker, S., McCave, I. N. & Elderfield, H. Surface and deep ocean coupling in the subpolar North Atlantic during the last 230 years. *Paleoceanography* **25**, PA2101 (2010).
52. Moffa-Sanchez, P., Born, A., Hall, I. R., Thornalley, D. J. R. & Barker, S. Solar forcing of North Atlantic surface temperature and salinity over the past millennium. *Nat. Geosci.* **7**, 275–278 (2014).
53. Thornalley, D. J. R., Elderfield, H. & McCave, I. N. Holocene oscillations in temperature and salinity of the surface subpolar North Atlantic. *Nature* **457**, 711–714 (2009).
54. Richter, T. O., Peeters, F. J. C. & van Weering, T. C. E. Late Holocene (0-2.4 ka BP) surface water temperature and salinity variability, Feni Drift, NE Atlantic Ocean. *Quat. Sci. Rev.* **28**, 1941–1955 (2009).
55. Morley, A. et al. Solar modulation of North Atlantic central water formation at multidecadal timescales during the late Holocene. *Earth Planet. Sci. Lett.* **308**, 161–171 (2011).
56. Morley, A., Rosenthal, Y. & deMenocal, P. Ocean-atmosphere climate shift during the mid-to-late Holocene transition. *Earth Planet. Sci. Lett.* **388**, 18–26 (2014).
57. Sicre, M.-A. et al. A 4500-year reconstruction of sea surface temperature variability at decadal time-scales off North Iceland. *Quat. Sci. Rev.* **27**, 2041–2047 (2008).
58. Joyce, T. M. & Zhang, R. On the path of the Gulf Stream and the Atlantic Meridional Overturning Circulation. *J. Clim.* **23**, 3146–3154 (2010).
59. Suman, D. O. & Bacon, M. P. Variations in Holocene sedimentation in the North American Basin determined from ^{230}Th measurements. *Deep-Sea Res.* **36**, 869–878 (1989).
60. Adkins, J. F., Boyle, E. A., Keigwin, L. & Cortijo, E. Variability of the North Atlantic thermohaline circulation during the last interglacial period. *Nature* **390**, 154–156 (1997).
61. Hodson, D. L. R., Robson, J. I. & Sutton, R. T. An anatomy of the cooling of the North Atlantic Ocean in the 1960s and 1970s. *J. Clim.* **27**, 8229–8243 (2014).

Extended Data Fig. 1 | Age model for core KNR-178-56JPC. a, ^{14}C and
[210]Pb dating. The ^{14}C ages (with 1σ ranges; grey, rejected dates) from
planktic foraminifera yield a modern core-top age and indicate an average
sedimentation rate over the past 1,000 years of 320 cm kyr^{-1} (dashed
line). The presence throughout the core of abundant lithogenic grains in
the >150-µm fraction—along with the coarse sortable-silt mean grain
size values—suggests that some reworking of foraminifera has probably
occurred, resulting in average ^{14}C ages that may be slightly (around
50 years) older than their final depositional age, consistent with the fact
that the ^{210}Pb dates do not splice smoothly into the ^{14}C ages (the ^{14}C ages
appear slightly too old). The final age model was therefore based on the
[210]Pb ages for the past century, and was then simply extrapolated back in
time using the linear sedimentation rate of 320 cm kyr^{-1}. Given that none
of our findings depend on close age control in the older section of this
core (that is, before AD 1880), this uncertainty (with converted ^{14}C ages
being about 50 years older than the extrapolated linear age model) does
not affect our conclusions. **b**, Left, the age model for the top 80 cm of core
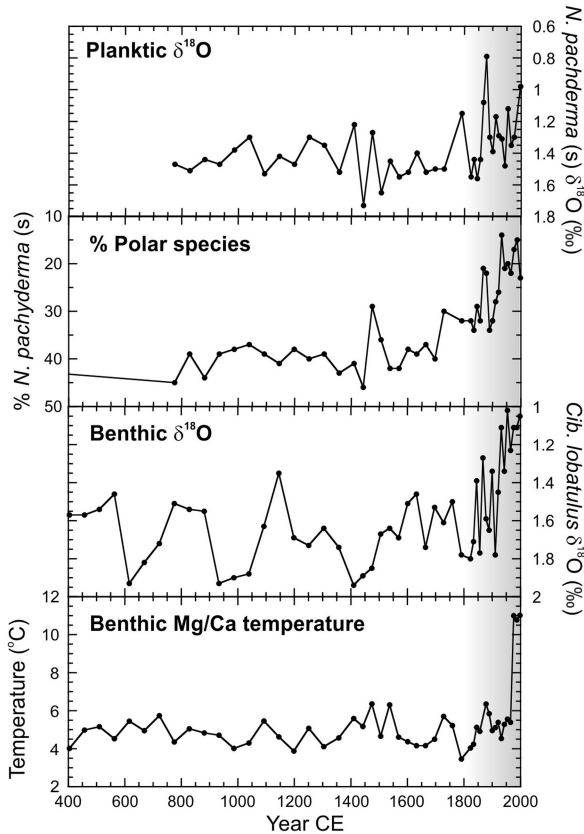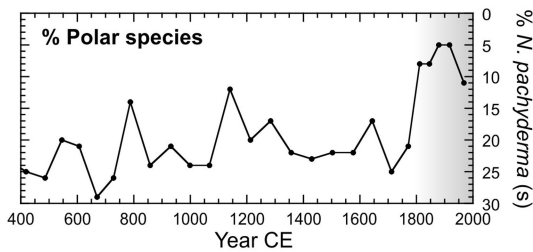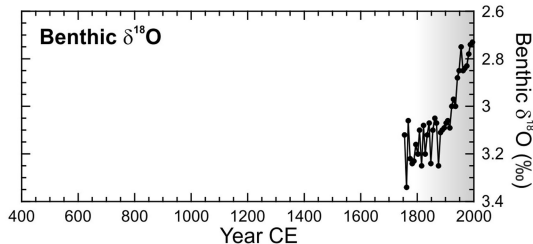56JPC is based on ^{210}Pb dating of bulk sediment, using the constant initial

concentration (CIC) method (rejecting the date at 47 cm, which probably
indicates a burrow). A simple two-segment linear fit to the ^{210}Pb dates is
adopted (rather than point-to-point interpolation or a spline) because
sedimentological evidence—an abrupt increase in the percentage of coarse
fraction at 23 cm depth, not observed elsewhere in the core—is indicative
of a step change in the sedimentation rate. Horizontal dashed lines denote
the depths of the segments at which the sedimentation rate is inferred
to change. Centre, further support for the age model of 56JPC over the
past century comes from the down-core abundance profile of spheroidal
carbonaceous particles (SCPs, derived from high-temperature fossil
fuel combustion, counted as described[39]), which ramped up from
the mid to late 1800s and peaked in the 1950s to 1970s (40 cm to 25 cm)
before declining over recent decades, consistent with the ^{210}Pb-based age
model. Right, the occurrence of ^{137}Cs in the top 40 cm or so of the core
is also consistent with the ^{210}Pb-based age of around 1950 at 40 cm.
The age uncertainty (1σ) for the past 60 years of the core is estimated
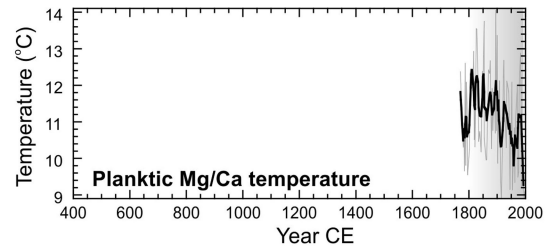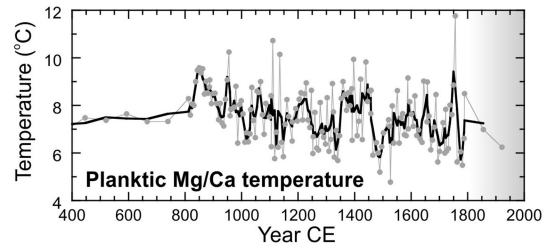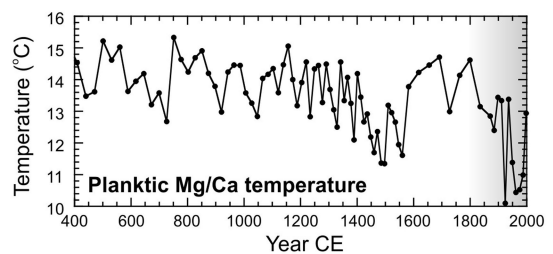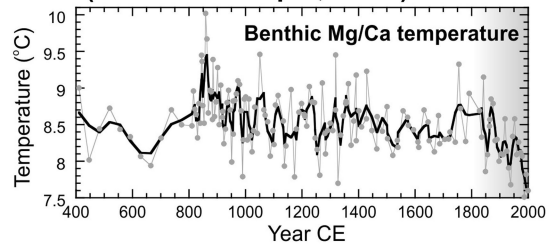at ±2–3 years. We note that the sediment core top is at 3 cm depth in the
core-liner.
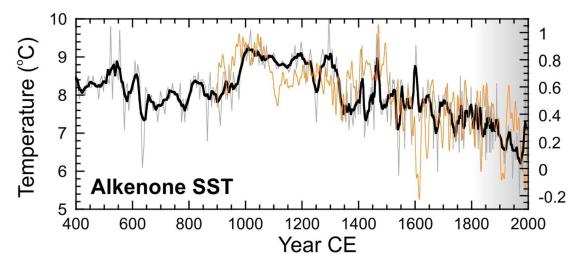
Extended Data Fig. 2 | Age models for additional cores. a, ^{14}C-based age model, derived from linear interpolation of ^{14}C-dated planktic foraminifera (with 1σ ranges) in sediment core KNR-178-48JPC (used for the $DWBC_{LSW}$ sortable-silt reconstruction), yielding a modern core-top age and an average sedimentation rate of around 50 cm kyr^{-1}. We note that the core top is at 3 cm depth in the core-liner. The inset shows the SCP profile for 48JPC on the basis of the ^{14}C age model, confirming the modern age of the top sediments, with SCPs showing the expected profile—increasing in concentration from the late 1800s onwards, peaking at around 1950 to 1970, and declining afterwards. **b,** Updated age model for core KNR-158-10MC (after ref. [47]; used in Extended Data Fig. 5 examining regional near-surface temperature trends in the Northwest Atlantic during the industrial era), using new ^{210}Pb dating (CIC method) for the top 7 cm and rejecting the anomalously old ^{14}C age at 4 cm depth; the inset shows

[210]Pb age constraints in the top 8 cm. A single detectable occurrence of ^{137}Cs at 2–2.5 cm (equivalent to 1957 on the ^{210}Pb-based age model) can be linked to the bomb peak at 1963, supporting the age model. Also, SCPs were found in the top 5 cm of this core, confirming the industrial-era age for the top 5 cm; however, the low concentrations of SCPs prevent meaningful interpretation of the down-core trends and are not shown. **c,** Age model for core OCE-326-MC29B (used for T_{sub} reconstruction of the Northwest Atlantic shelf): [14]C ages of planktic foraminifera (with 1σ ranges), from ref. [48]. Support for this age model is provided by the SCP concentrations (inset; this study), which show the expected down-core profile[39] when plotted using the ^{14}C ages. [210]Pb dating[48] also suggests a sedimentation rate of around 120 cm kyr^{-1} for the uppermost sediments, consistent with the ^{14}C ages and SCP profile.
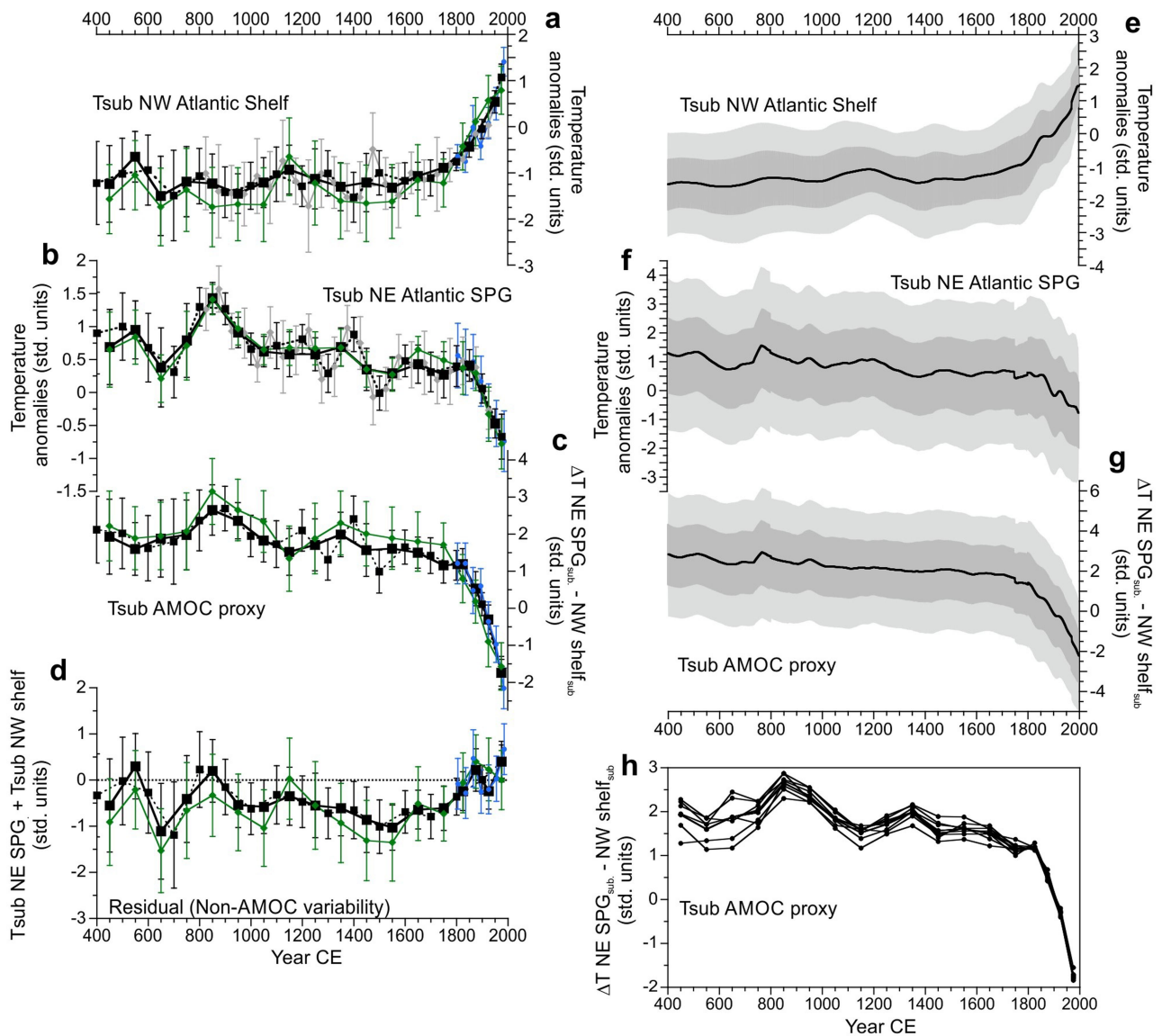
NW ATLANTIC SLOPE

a Emerald Basin (29MC, 250m water depth, site 2)

Planktic $\delta^{18}O$

% Polar species

Benthic $\delta^{18}O$

Benthic Mg/Ca temperature

b Laurentian Fan (13MC, site 3)

% Polar species

c Gulf of St Lawrence (409m water depth, site 1)

Benthic $\delta^{18}O$

NE ATLANTIC SPG

d Gardar drift (site 4)

Planktic Mg/Ca temperature

e Bjorn drift (site 5)

Planktic Mg/Ca temperature

f Feni drift (site 6)

Planktic Mg/Ca temperature

g ENACW, formed in eastern SPG (899m water depth, site 7)

Benthic Mg/Ca temperature
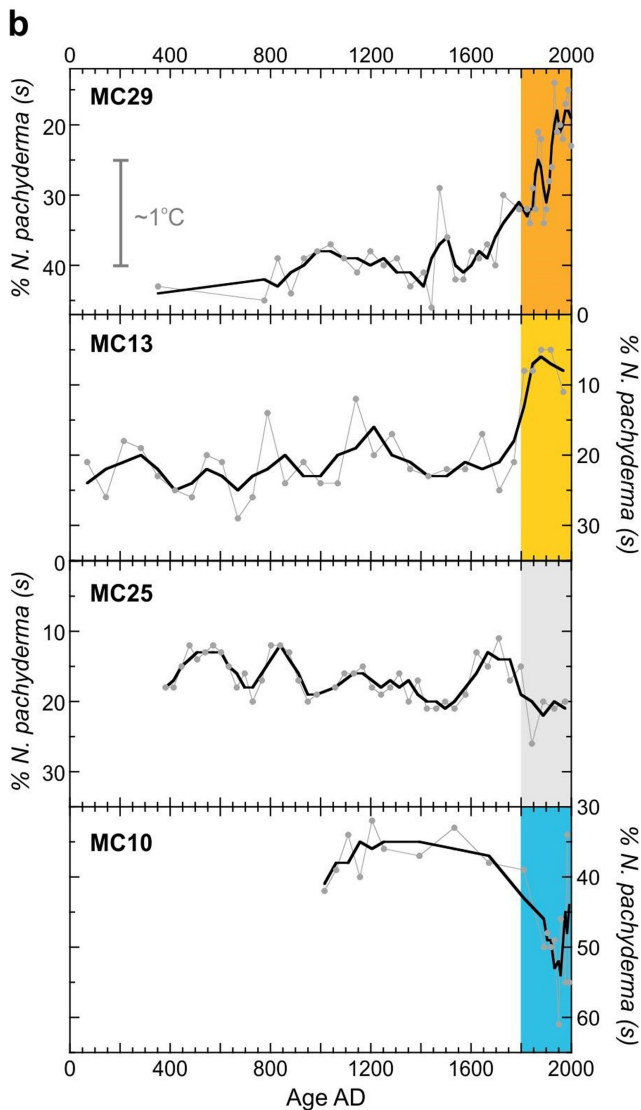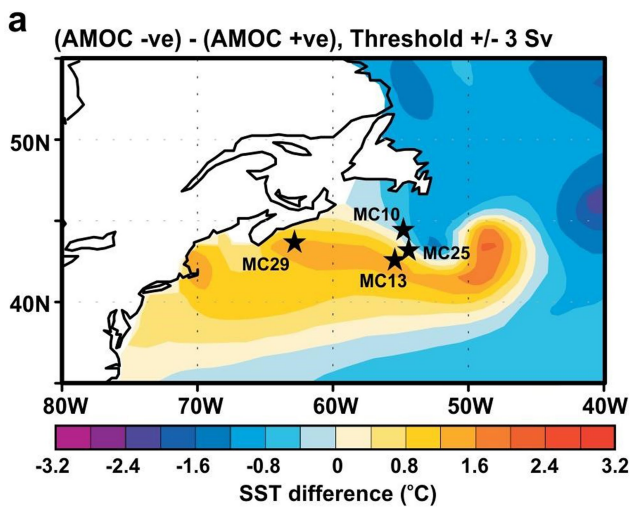
h *North Iceland shelf/Rahmstorf SPG SST

Alkenone SST

Extended Data Fig. 3 | Raw data for construction of the T_{sub} AMOC proxy shown in Fig. 3. Locations are shown in Fig. 2b. **a–c**, Temperature proxy records[48–50] used for the Northwest Atlantic stack (Emerald Basin, Laurentian Fan and Gulf of St Lawrence), where model studies[11,12] indicate that AMOC weakening results in warming of surface and subsurface waters. **d–g**, Records used to reconstruct Northeast Atlantic SPG subsurface temperatures: **d**, Gardar drift[51]; **e**, combined South Iceland data (Bjorn drift)[52,53]; **f**, Feni drift[54]; **g**, Eastern North Atlantic Central

Water (ENACW), largely composed of waters formed in the eastern SPG[55,56]. **h**, The high-resolution alkenone sea-surface temperature (SST) record from the North Iceland shelf[57] was not included because it is not located within the open North Atlantic SPG (although it does also show, like the other Northeast Atlantic records, that the lowest temperature of the past 1,600 years occurred during the most recent century). Also shown for reference is the Rahmstorf central SPG SST reconstruction (based largely on terrestrial proxies)[6].
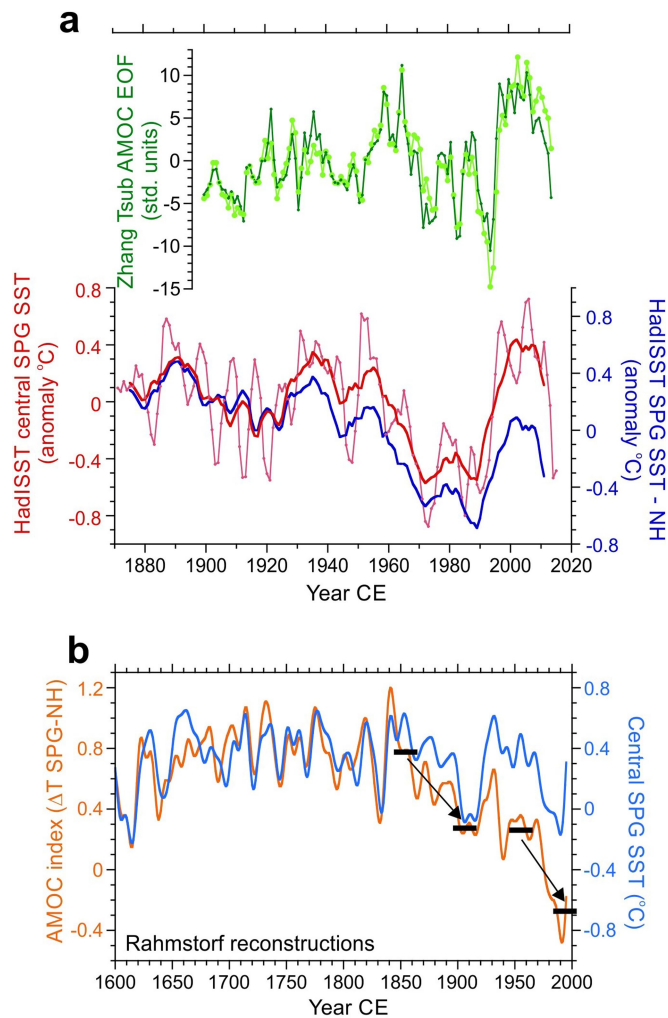
Extended Data Fig. 4 | Different binning and averaging approaches and the residual temperature signal. a, **b**, Stacked, normalized proxy temperature data (T_{sub}) from the Northwest Atlantic shelf/slope (**a**) and Northeast Atlantic SPG (**b**). **c**, The derived T_{sub} AMOC proxy, calculated as the numerical difference between the stacks shown in **a** and **b**. **d**, The residual temperature variability in stacks **a** and **b** that is not described by the (anti-phased dipole) T_{sub} AMOC proxy shown in **c**—that is, the in-phase temperature variability common to both stacks, calculated as the numerical sum of the two stacks (if divided by two, this would be the numerical mean). This represents the inferred non-AMOC-related temperature variability common to both regions, and broadly resembles Northern Hemisphere temperature reconstructions, most notably colder residual temperatures during the LIA, around 1350 to 1850. For **a**–**d**, black solid lines and squares represent preferred binning (50 years for 1800–2000;
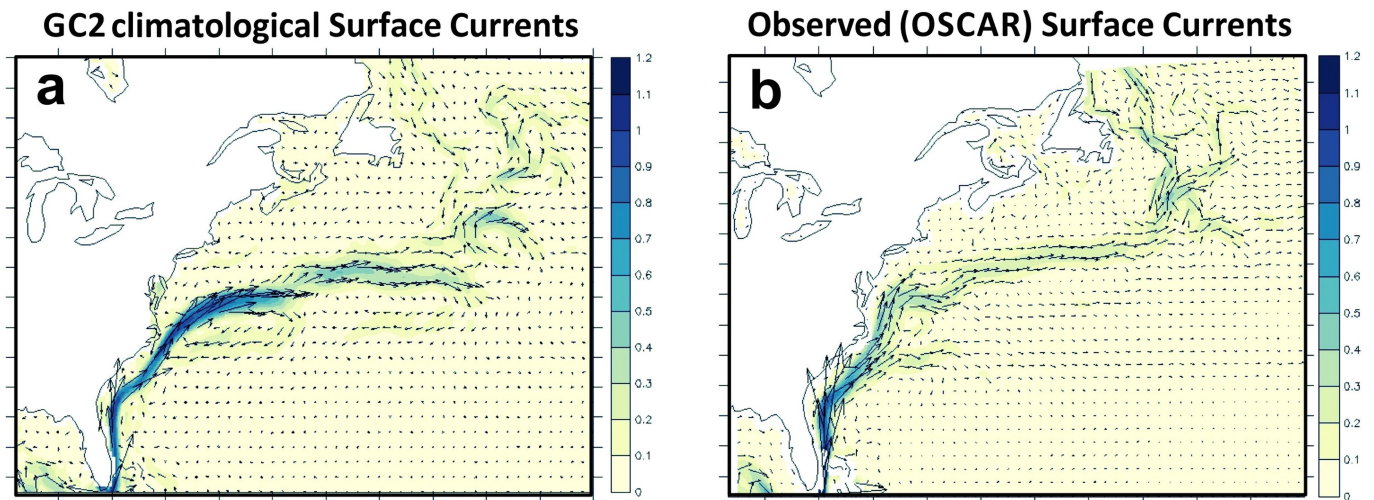
100 years for 400–1800); green line and symbols, as for preferred binning, but with stacks produced by first binning the proxy data at each site and then averaging these binned site values, as opposed to binning all the proxy data together in one step (the former ensures equal weighting for each site, the latter biases the final result to the higher-resolution records); black dashed lines and symbols, 100-year bins offset by 50 years from the preferred bins; grey lines and symbols, 50-year bins (not shown for **c** and **d**); blue lines and symbols; 30-year bins for 1790–2000. Error bars for **a**–**d** are ±2 s.e. **e**–**g**, As for **a**–**c**, except using a Monte Carlo approach and published uncertainties for age assignment and temperature reconstructions; light and dark grey shading represent ±1σ and ±2σ, respectively. **h**, Jackknife version of **c**, with each line representing the T_{sub} AMOC proxy but leaving out one of the individual proxy records each time.

Extended Data Fig. 5 | SST response of the Northwest Atlantic to AMOC weakening. a, Modelled SST difference between a weak (negative) and strong (positive) AMOC[58]. This pattern is model-dependent, with the study cited here[58] chosen because of its good agreement with observations of Gulf Stream variability. The locations of cores used for panel **b** are shown by black stars. **b**, Percentage abundances of the polar species *N. pachyderma* (sinistral) in marine sediment cores from the Northwest Atlantic, as an indicator of near-surface (around 75 m) temperatures. A 15% increase indicates around 1 °C of cooling (we note the reversed *y* axes). The opposing trends over the past 200 years are consistent with the SST pattern modelled for a weakening of the AMOC, as shown in panel **a**. Data and age models for the cores are: OCE326-MC29[48] using the original ^{14}C dating and as shown in Extended Data Fig. 2; OCE326-MC13 and OCE326-MC25[49] using the original ^{14}C age ties at the top and bottom of the core and scaling the intervening sedimentation rate to the percentage of CaCO$_3$ content[49,59,60]; KNR158-MC10, this study, using the age model in Extended Data Fig. 2.
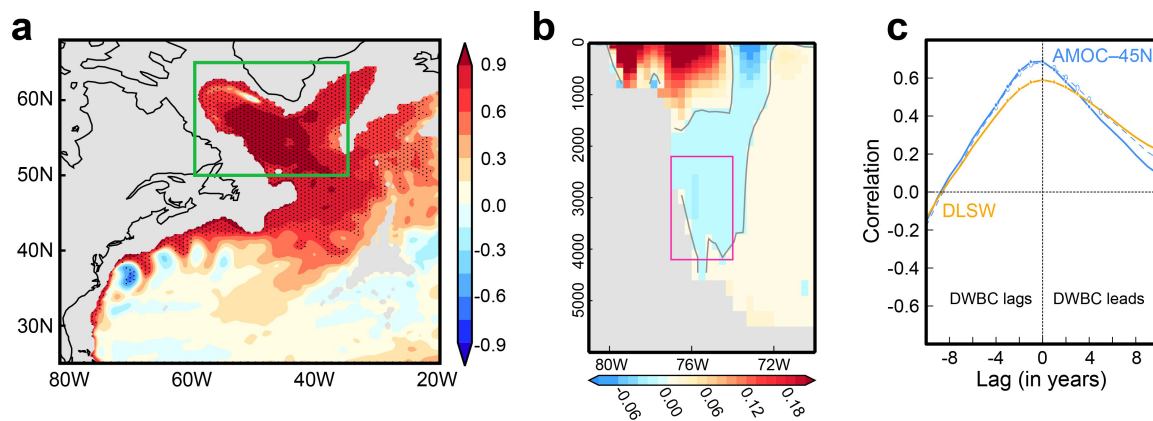
Extended Data Fig. 6 | Temperature fingerprints of the AMOC during the twentieth century. a, Top, T_{sub} AMOC fingerprint[11] obtained using empirical orthogonal function (EOF) analysis of the EN4 dataset (light green, the leading mode (EOF1) of T_{sub} variability from 1993–2003, as defined by Zhang[11], applied to the EN4 data; dark green, the second mode of T_{sub} variability (EOF2) of the North Atlantic for 1900–2015, equivalent to the EOF1 defined for 1993–2003). No substantial twentieth-century AMOC decline is seen in this observation-based reconstruction. Bottom, instrument-based reanalysis of the 'cold blob' central SPG region (red; 3-year (thin line) and 11-year (thick line) smoothing; 47° N to 57° N, 30° W to 45° W) used in the Rahmstorf SST AMOC proxy[6]. The data are from the HadISST project. The reconstructed central SPG SST bears some resemblance to the T_{sub} AMOC fingerprint record, which is not unexpected given that the central SPG forms a substantial spatial component of the T_{sub} fingerprint. No clear decrease is shown in the central SPG SST, and the equivalent Rahmstorf AMOC proxy[6] (blue; central SPG minus the Northern Hemisphere (NH) temperature) declines during the twentieth century because of the subtraction of the NH warming trend. **b**, Reconstructed (predominantly terrestrial-based) AMOC proxy (orange; the temperature difference between the central SPG and the NH) and the central SPG SST reconstruction[6] (blue). There is a two-step decline in the AMOC proxy, at 1850–1900 and 1950–2000—the former being mainly the result of a strong cooling of the SPG (which probably weakened northward heat transport, paralleling the weakening shown by our DWBC proxy), and the latter being due mainly to subtraction of the strong NH warming trend, rather than a persistent SPG cooling.
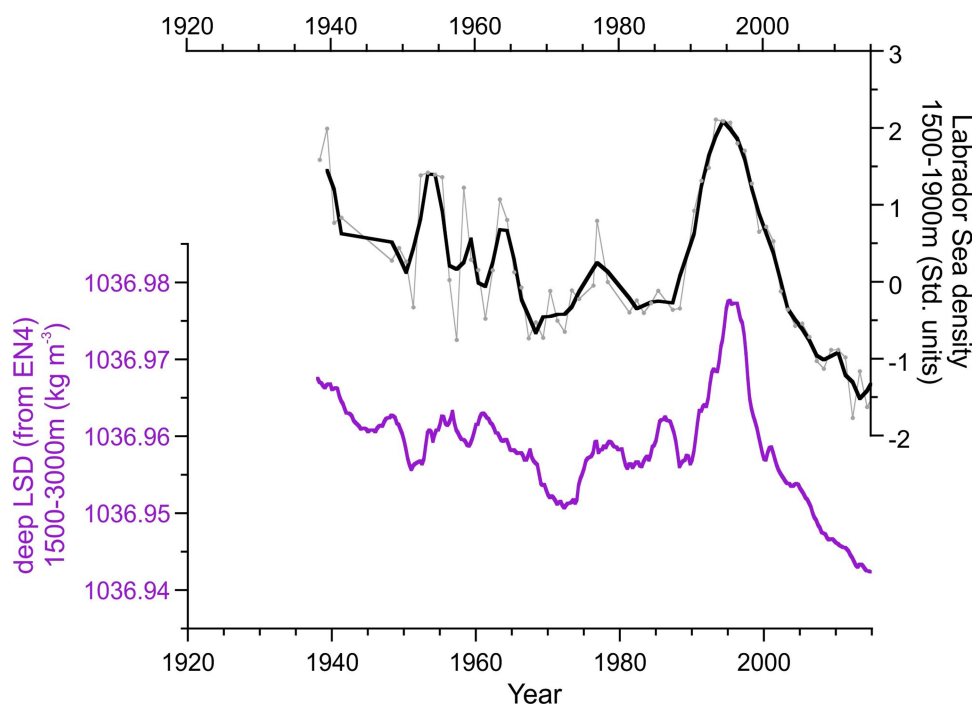
GC2 climatological Surface Currents

Observed (OSCAR) Surface Currents

Extended Data Fig. 7 | DWBC changes in model HadGEM3-GC2. a, b, Climatological surface current direction (in arrows) and speed (shaded, m s^{-1}) obtained from the control simulation with HadGEM3-GC2 and the satellite product OSCAR.

Extended Data Fig. 8 | Modelled link between DWBC velocity, DLSD and AMOC in the HiGEM model. a, Correlation (colour bar) of the vertically averaged ocean density (at 1,000–2,500 m) with the DLSD index (as defined in ref. [4]; green box, 1,000–2,500 m average) in a 340-year present-day control run of the HiGEM model (see ref. [36]). **b**, Climatology of the modelled meridional ocean velocity (in m s^{-1}) averaged between 30° N and 35° N, illustrating the modelled position of the DWBC. The
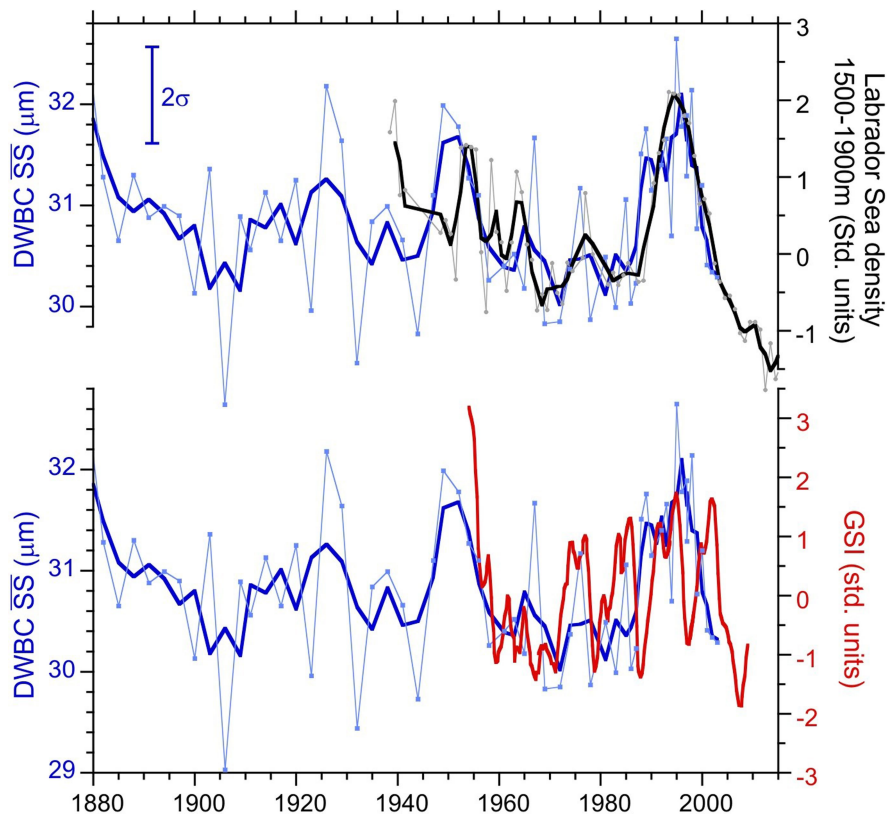
y axis shows the water depth in metres. **c**, Cross-correlations between the modelled average DWBC flow speed in the pink box in panel **b** and indices of DLSD and AMOC at 45° N (the dashed line omits the Ekman component). We note that the box over which the DWBC flow index in panel **c** is averaged has changed with respect to Fig. 1, in order to take into account of the fact that the return flow is deeper in the HiGEM model than in HadGEM3-GC2.

Extended Data Fig. 9 | Comparison of Labrador Sea density parameters. The model-based DLSD parameter—proposed in ref. [4] and using the EN4 reanalysis dataset—incorporates a larger area and greater depth range than do instrumental-data-only studies, such as ref. [5], which examines past variability in Labrador Sea convection and focuses on the central Labrador Sea and on depths less than 2,000 m, where most observational data are available. The comparison here of DLSD (purple line, three-year mean) from the EN4 dataset with instrumental data on density changes in the central Labrador Sea at 1,500–1,900 m depth (grey line, annual averages; black line, three-year mean) illustrates that the two parameters show very similar variability. Both are dominated by the density changes caused by deep convection in the Labrador Sea, which can reach down to around 2,000 m. Estimates of uncertainty are discussed in ref. [61].

Extended Data Fig. 10 | Comparison with Gulf Stream Index (GSI).
A direct influence of the changing position of the Gulf Stream on the grain size of our core sites can be ruled out by comparing instrumental records of the Gulf Stream position (red, GSI[58]) with the down-core sortable-silt (SS) mean grain size data in 56JPC (blue; thicker line is three-point smoothed). There is no clear correlation between these two proxies (bottom). However, there is a coupling between our SS data (which represent inferred $DWBC_{LSW}$ flow speed) and density changes in the deep Labrador Sea (grey, annual; black, three-point smoothed; top panel). The 2σ SS error bar ($n = 30$) is for the three-point mean.